Capillary adhesion at the nanometer scale

Shengfeng Cheng[1,2,*] and Mark O. Robbins[1,†]

[1]*Department of Physics and Astronomy, Johns Hopkins University, 3400 N. Charles Street, Baltimore, Maryland 21218, USA*

[2]*Department of Physics, Virginia Polytechnic Institute and State University, Blacksburg, Virginia 24061, USA*

Molecular dynamics simulations are used to study the capillary adhesion from a nonvolatile liquid meniscus between a spherical tip and a flat substrate. The atomic structure of the tip, the tip radius, the contact angles of the liquid on the two surfaces, and the volume of the liquid bridge are varied. The capillary force between the tip and substrate is calculated as a function of their separation h. The force agrees with continuum predictions based on macroscopic theory for h down to $\sim$5 to 10 nm. At smaller h, the force tends to be less attractive than predicted and has strong oscillations. This oscillatory component of the capillary force is completely missed in the macroscopic theory, which only includes contributions from the surface tension around the circumference of the meniscus and the pressure difference over the cross section of the meniscus. The oscillation is found to be due to molecular layering of the liquid confined in the narrow gap between the tip and substrate. This effect is most pronounced for large tip radii and/or smooth surfaces. The other two components considered by the macroscopic theory are also identified. The surface tension term, as well as the meniscus shape, is accurately described by the macroscopic theory for h down to $\sim$1 nm, but the capillary pressure term is always more positive than the corresponding continuum result. This shift in the capillary pressure reduces the average adhesion by a factor as large as 2 from its continuum value and is found to be due to an anisotropy in the pressure tensor. The component in the plane of the substrate is consistent with the capillary pressure predicted by the macroscopic theory (i.e., the Young-Laplace equation), but the normal pressure that determines the capillary force is always more positive than the continuum counterpart.

I. INTRODUCTION

Adhesion and friction due to capillary forces affect the flow and yield properties of granular materials in dramatic ways [1–4]. One example is that the strength of powders can be greatly enhanced by absorbing moisture from the ambient atmosphere [5]. This fact was known to our ancient ancestors when they built walls from clay mixed with an appropriate amount of water. The meniscus formed between clay particles binds them together with capillary forces, increasing the unconfined yield strength of the granular assembly. The same physics is involved when wet sand is used to build sand castles, which would not be possible to make with dry sand [6–10].

As dimensions shrink into the nanoscale, capillary forces become increasingly important and can be the dominant source of adhesion between surfaces [11–13]. For example, they often prevent micro- or nanoelectromechanical systems from functioning under ambient conditions or lead to damage in their fabrication processes [14]. They play a major role in nanoscopic sliding friction and lead to a nontrivial velocity dependence of friction [15–19]. Many previous experiments also show that when an atomic force microscope (AFM), or more generally any small probe, is used to examine a hydrophilic surface in a humid environment, a major contribution to the tip-surface interaction is from the capillary forces associated with the water meniscus bridging the tip and surface [15,20–28]. The geometry in these experiments can be reasonably approximated as a liquid bridge connecting a spherical tip of certain size and a flat surface. Though there can be a complex

interplay between the tip shape and capillary forces [20,29], the simple sphere-on-flat geometry serves as a prototype to understand more realistic situations. These include particle-surface or particle-particle interactions occurring in many physical, chemical, and biological processes [30].

A capillary bridge can form either by capillary condensation or by accumulation of liquid [31,32]. The former occurs when multilayer adsorption from a vapor proceeds to the point at which a small gap, such as the one between the tip and sample surfaces, is filled with liquid separated from the vapor phase by a meniscus [33]. Here the presence of the surfaces shifts the phase diagram of the fluid to favor the liquid phase [14]. Capillary condensation is responsible for the formation of water menisci in the AFM experiments mentioned above [15,20–28]. The capillary pressure inside the liquid bridge is fixed by the relative humidity of the vapor phase, and the volume of the liquid bridge depends on the size of the gap. Capillary condensation also occurs in liquid crystals [34,35], aqueous mixtures of polymers [36,37], and model fluid mixtures [38] when confined in small gaps.

A capillary bridge can also form by accumulation of liquid. For example, insects excrete fluid to create adhesion that allows them to walk on walls or ceilings. In this case and many other occasions, a nonvolatile liquid is used in order to avoid the quick dry out of the liquid [5,39–41]. When the liquid only partially wets the solid surfaces, the volume of the liquid bridge is controlled by the amount of liquid injected. The bridge volume and the wetting properties of the solid surfaces then determine the shape of the liquid bridge and the capillary pressure. In this case the volume of the liquid bridge acts as a controlling parameter and determines the capillary forces [10,42].

The macroscopic theory of capillarity [43], which is briefly introduced in the next section, is routinely used to calculate

*chengsf@vt.edu

†mr@pha.jhu.edu

capillary forces and interpret experiments, even at nanometer scales. However, new effects are expected to become important for liquid bridges with submicron dimensions. Continuum theories often introduce a disjoining pressure that reflects the variation in interfacial free energy with the thickness of the fluid due to van der Waals interactions [44–46]. The discrete structure of fluids becomes important as the thickness shrinks to a few nanometers. Molecules form discrete layers that lead to rapid oscillations in free energy and disjoining pressure with thickness [47–50].

In this paper, we use molecular dynamics (MD) simulations to study the capillary forces produced by a small liquid bridge connecting a spherical tip and a flat substrate. Our goal is to address the fundamental limits of macroscopic theory and to develop understanding of new behavior that enters at the nanometer scale. We find that the interface shape and the interfacial contribution to the capillary force are surprisingly close to continuum predictions in all cases. However, the total capillary force is strongly affected by molecular layering and pressure anisotropy when the separation between surfaces is less than a few nanometers.

The next section briefly describes the macroscopic theory. Section III describes our simulation techniques and geometries. Section IV presents results for a wide range of cases and the final section presents a summary and conclusions.

II. MACROSCOPIC THEORY OF CAPILLARY FORCES

The geometry of the system studied in this paper is sketched in Fig. 1(a), where a liquid meniscus bridges between a
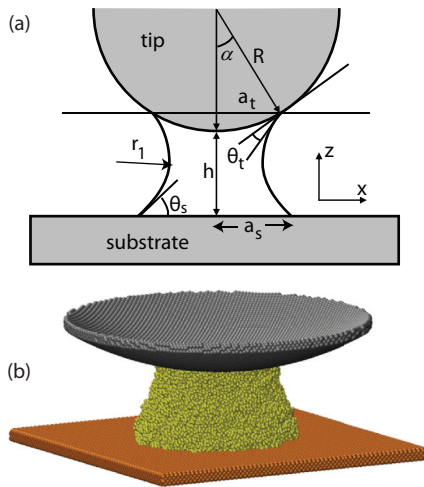

FIG. 1. (Color online) (a) Geometry of a liquid bridge between a sphere and a substrate, including contact angles θ_i and radii a_i at the intersection of the meniscus with the tip ($i = t$) and substrate ($i = s$). The pressure drop is related to the radii of curvature through Eq. (1). The radii are negative when the center of the circle is outside the drop, as for r_1 in the figure. (b) A snapshot from simulations of a liquid bridge (yellow) between a spherical tip (gray) and an atomically flat substrate (orange). Here the tip was made by bending a thin fcc crystal with a (001) surface into a sphere with radius $R = 100\sigma$, where $\sigma \sim 0.5$ nm is a molecular diameter. The bridge intersects the tip with radius $a_t \approx 25\sigma$. Only the central parts of the substrate and tip are shown.

spherical tip and a flat surface. In the macroscopic theory, the pressure change Δp across a curved liquid-vapor interface (or, more generally, a fluid-fluid interface) satisfies the Young-Laplace equation:

$$\Delta p = \gamma(1/r_1 + 1/r_2) \equiv 2\gamma\overline{\kappa}, \qquad (1)$$

where γ is the liquid-vapor interfacial tension, r_i the principal radii of curvature, and $\overline{\kappa}$ the mean curvature. We take Δp to be negative when the interior of the drop has a lower pressure. Then r_i is negative when the center of the corresponding circle is away from the drop as for r_1 in Fig. 1(a).

For micrometer and smaller drops, pressure changes due to gravity can be neglected. The equilibrium interface must then have a constant mean curvature so that the pressure is constant in both the liquid and vapor phases. The interface must also intersect solid walls at a contact angle θ determined by the Young equation:

$$\gamma \cos\theta = \gamma_{sv} - \gamma_{sl}, \qquad (2)$$

where γ_{sv} and γ_{sl} are the solid-vapor and solid-liquid interfacial tensions, respectively. The Young equation represents a balance of tangential forces on the contact line where all three phases meet [44,51].

The shape of the liquid bridge between a spherical tip and a flat substrate is uniquely determined by Δp, the tip-substrate separation h, and the contact angles θ_t and θ_s of the liquid on the tip and substrate surfaces, respectively. Our MD results were compared to the exact solution of Orr *et al.* for Eq. (1) in terms of elliptic integrals [52]. Simpler analytic solutions are also widely used in analyzing experimental data [30,53–57], but are only valid in limiting cases such as $|r_2| \gg |r_1|$ or constant r_1.

For nonvolatile liquids, Δp is fixed by the total volume V_l of the liquid drop. Volatile liquids can condense or evaporate until the chemical potential of molecules in the gas and liquid phases is equal. The value of Δp then satisfies the Kelvin equation that relates Δp to the relative humidity of the vapor. We will consider the nonvolatile case because of the ease of equilibration. The results for volatile liquids are the same for a given interface geometry, but the variation of Δp with h is different in the two cases.

In the macroscopic continuum picture there are two contributions to the capillary force F_{cap} between the solids [58]. The first comes directly from the interfacial tension exerted by the meniscus on the contact line where it contacts the solid. This force is always attractive in the geometries considered, and we will choose our sign convention so that an attractive force has a negative value. The second contribution comes from the integral of the Laplace pressure over the area where the drop contacts the solid. This force is attractive when Δp is negative. Because of the azimuthal symmetry of the system about the vertical axis through the sphere center, only the component of the force along this axis is nonzero and the interface intersects the tip and substrate at circles of radius a_t and a_s, respectively. The sum of the meniscus and Laplace contributions gives

$$F_{cap} = -2\pi\gamma a_i \sin\phi_i + \pi a_i^2 \Delta p, \qquad (3)$$

where ϕ_i is the angle relative to the x-y plane of the tangent to the liquid-vapor interface at the solid surface. At the substrate $\phi_s = \theta_s$, while on the spherical tip of radius R,

$\phi_t = \theta_t + \alpha$, where $\alpha = \arcsin(a_t/R)$ [Fig. 1(a)]. Newton's third law requires that the magnitudes of the capillary force on the tip and substrate are the same. For a case like Fig. 1(b), the Laplace pressure acts on a smaller projected area at the tip surface than at the substrate surface (i.e., $a_t < a_s$), but this difference is compensated for by the differences in ϕ_i and a_i.

Many experiments are in the limit where the drop dimensions are much smaller than the tip radius, but much larger than the separation h. In this limit ($R \gg |r_2| \gg |r_1|$), F_{cap} is independent of both h and the drop volume V_l [30]. As V_l increases, the increases in a_t and a_s are compensated for by the decrease of $\overline{\kappa}$ and thus Δp. This condition frequently applies for granular materials held together by liquid bridges formed via capillary condensation, making their mechanical properties relatively insensitive to the relative humidity of the environment or the addition of extra nonvolatile liquids [10,21]. However, our simulations are generally in a different limit where the drop and tip have comparable dimensions and F_{cap} depends on both h and V_l.

Previous work has tested some aspects of the macroscopic theory down to atomic scales. For example, the Kelvin equation is obeyed by cyclohexane or water menisci with radii of curvature as small as 4 nm [59–63]. MD simulations confirmed that the Young-Laplace and Young equations hold down to a similar length scale for simple model potentials [51,64,65]. Grand canonical Monte Carlo simulations have also been used to investigate capillary condensation and to calculate capillary forces [66,67]. However, the latter studies used lattice models on square or cubic grids that may not capture the nanoscale behavior of atoms and molecules. To the best of our knowledge, there are no MD simulations reported on capillary condensation. One reason is that it is extremely difficult to study the thermal equilibration of a liquid-vapor system with MD.

III. SIMULATION METHODS

Figure 1(b) shows a snapshot of a liquid bridge that connects a spherical tip and a flat substrate. The liquid partially wets both the tip and substrate surfaces. In our simulations, the gap width h between the tip and substrate is controlled and the bridge-induced capillary force F_{cap} between the two is calculated as h is varied.

Since our goal is to address generic behavior, we use a simple model potential that captures many aspects of the behavior of hydrocarbon chains [68–73]. Fluid molecules are modeled as short linear chains of four spherical beads. All beads, except those pairs directly bonded in one molecule, interact with a Lennard-Jones (LJ) potential

$$V_{LJ}(r) = 4\epsilon[(\sigma/r)^{12} - (\sigma/r)^6 - (\sigma/r_c)^{12} + (\sigma/r_c)^6], \quad (4)$$

where r is the distance between beads and σ represents an effective molecular diameter where the potential energy changes sign. The LJ potential is truncated and shifted at a cutoff radius $r_c = 2.2\sigma$. The binding energy ϵ, diameter σ, and mass m of the beads are used to define all dimensions.

The neighboring beads in each chain interact through a purely repulsive LJ potential with $r_c = 2^{1/6}\sigma$ and an attractive finitely extensible nonlinear elastic (FENE) potential [68]

$$V_{FENE}(r) = -\tfrac{1}{2}KR_0^2\ln[1 - (r/R_0)^2], \quad (5)$$

with the canonical values of $R_0 = 1.5\sigma$ and $K = 30\epsilon/\sigma^2$. Monatomic LJ systems have a very high vapor pressure and are not well suited for studies of liquid-gas interfaces [74]. Increasing the chain length to four beads leads to a negligible vapor pressure without significantly increasing the molecular size or slowing down the dynamics. We have verified that increasing the chain length to eight beads does not change any of the conclusions reached below.

To provide a rough mapping of our results to experiments we use the facts that a typical hydrocarbon has surface tension $\gamma \sim 25$ mN/m and the separation between molecules corresponds to a chain diameter $\sigma \sim 0.5$ nm. In our simulations the surface tension is calculated with the Kirkwood-Buff expression for a flat liquid-gas interface [75]. The fluid is kept at a constant temperature of $T = 0.7\epsilon/k_B$ that corresponds to the melting temperature of a pure LJ system [76] and is about twice the glass transition temperature of FENE chains [77]. The calculated value of surface tension is $\gamma = 0.88\epsilon/\sigma^2$, which implies $\epsilon \sim 7 \times 10^{-21}$ J $\simeq 0.044$ eV. The temperature also maps to a reasonable value of ~ 360 K. Since the bead diameter of 0.5 nm corresponds to three to four carbons along the backbone [68], $m \sim 10^{-25}$ kg. The characteristic LJ time, $\tau = \sqrt{m\sigma^2/\epsilon}$, is then of the order of 2 ps. The unit of pressure is $\epsilon/\sigma^3 \sim 56$ MPa and the unit of force is $\epsilon/\sigma \sim 14$ pN. Plotted forces in the following figures are normalized by $10^2\epsilon/\sigma \sim 1.4$ nN. All the mappings of LJ and real units are summarized in Table I.

The substrate is treated as either an elastic or rigid solid. Atoms in the substrate form an fcc lattice with a (001) surface. The nearest-neighbor spacing is $d = 2^{1/6}\sigma$. For the elastic substrate, nearest neighbors interact through a harmonic potential

$$V(r) = \tfrac{1}{2}k(r - d)^2, \quad (6)$$

with $k = 228\epsilon/\sigma^2$. This substrate corresponds to a solid with LJ interactions at the strength of 4ϵ and a Young's modulus of about $240\epsilon/\sigma^3$ [78,79]. Given the mapping above, this modulus is about 14 GPa, which means that our elastic substrate is stiffer than typical hydrocarbon solids, but much softer than the tip-substrate pairs in most AFM experiments. The elastic substrate has dimensions $190.49\sigma \times 190.49\sigma \times 7.94\sigma$ with periodic boundary conditions imposed in the x-y plane. The

TABLE I. Rough mapping between LJ and real units. Plotted forces are normalized by $10^2\epsilon/\sigma \sim 1.4$ nN.

Physical quantity	LJ unit	SI value
Energy	ϵ	7×10^{-21} J
Length	σ	0.5×10^{-9} m
Mass	m	1×10^{-25} kg
Time	τ	2×10^{-12} s
Force	ϵ/σ	1.4×10^{-11} N
Surface tension	ϵ/σ^2	2.8×10^{-2} N/m
Pressure	ϵ/σ^3	5.6×10^7 N/m^2
Temperature	ϵ/k_B	5.1×10^2 K

depth has little effect on the results, for reasons discussed in the next section. For the rigid substrate, the thickness can be reduced to include only those atoms that are within the interaction range of the fluid.

The tip is modeled as a rigid sphere. The radius R is varied from $25\sigma \sim 13$ nm, corresponding to a sharp AFM tip, up to infinity, corresponding to a flat surface. The atomic scale structure of the tip is also varied, since this profoundly affects the contact between the tip and substrate, either bare or with an adsorbed layer [78,80,81]. Some tips are made by bending three (001) planes of an fcc crystal with nearest-neighbor spacing d' into a spherical shape. The case $d' = d$ will be referred to as a commensurate tip, since its period matches that of the substrate. A denser tip with $d' = 0.944\,37d$ is referred to as incommensurate. We also make tips by cutting a spherical shell out of an fcc crystal that has the same structure as the substrate, or an amorphous solid with a density $1.0m/\sigma^3$. The former is called a stepped tip since it has a terraced surface, and the latter is called an amorphous tip. In all cases, the thickness of the shell is reduced to include only atoms that are within the interaction range of the fluid. A purely repulsive LJ potential (i.e., $r_c = 2^{1/6}\sigma$) is used for the direct interaction between the tip and substrate, but this interaction never contributes to the total force in the cases shown below since the separation between the tip and substrate atoms is always larger than r_c.

The equilibrium contact angle θ is controlled by changing the interactions between the liquid and solid. Fluid beads and solid atoms interact with a LJ potential [Eq. (4)] with modified energy and length scales, ϵ_{fs} and σ_{fs}, respectively. Unless noted, the simulations presented below use $\epsilon_{fs} = 0.8\epsilon$ and $\sigma_{fs} = 1.2\sigma$, and the potential is truncated and shifted at $r_c = 1.8\sigma_{fs} = 2.16\sigma$. As discussed next, this combination of ϵ_{fs} and σ_{fs} leads to a contact angle $\theta \sim 75°$ for our crystalline substrate. Increasing ϵ_{fs} favors wetting of the solid and decreases θ. Where noted, we also show results for commensurate tips with $\epsilon_{fs} = 1.08\epsilon$, which yields $\theta \sim 12°$ for our substrate. A further increase in ϵ_{fs} to 1.2ϵ leads to complete wetting (i.e., $\theta \to 0$) and the liquid film spreads over the entire substrate.

FIG. 3. (Color online) Final contact angle θ^f as a function of the initial angle θ^i for different solid surfaces and liquid geometries. For the fcc crystal with the nearest-neighbor spacing $d = 2^{1/6}\sigma$ (i.e., for the substrate, the commensurate tip, and the stepped tip), results are shown for both a liquid cylinder (circle) or a circular drop (filled triangle). Cylinder results are shown for the amorphous solid (open square) and the fcc crystal with the nearest-neighbor spacing $d' = 0.944\,37d$ (filled square), i.e., for the amorphous and incommensurate tips, respectively.

Figure 2 illustrates the geometries used to calculate θ. A circular drop or cylinder of liquid is placed on a flat substrate with the desired structure and interactions. Contact angles are obtained by fitting the liquid-vapor interface to a sphere or cylinder and finding the angle at the solid-liquid interface. The initial drop or cylinder makes an angle θ^i with the solid. The relaxation of the drop or cylinder is followed and the final angle θ^f is calculated and taken as θ. As shown in Fig. 3, θ^f is independent of θ^i. At the macroscopic scale, disorder and other effects usually lead to a dependence of θ^f on initial conditions known as contact angle hysteresis [44]. Any hysteresis in our simulations is less than the error bars ($\sim 1°$–$2°$) in θ^f.

Some continuum treatments include an additional energy equal to the length of the contact line times a line tension [82–84]. A positive line tension would favor a decrease in the circumference of a circular drop, leading to a larger contact angle than for a cylinder. The calculated θ is the same for both geometries, implying that the line tension has negligible effect. Line tension may become important as the drop radius decreases to a few σ, but we will focus on capillary bridges that are at least as wide as the drops used to find θ.

The contact angles for tips with different atomic structures are calculated using flat surfaces with the corresponding structure (Table II). In principle, the contact angle may change when a surface is bent into a sphere, but tests indicated that any change is within the error bars in θ for the tip radii $R \geqslant 25\sigma$ used here. In Fig. 3, $\theta = 75°$ for the substrate and
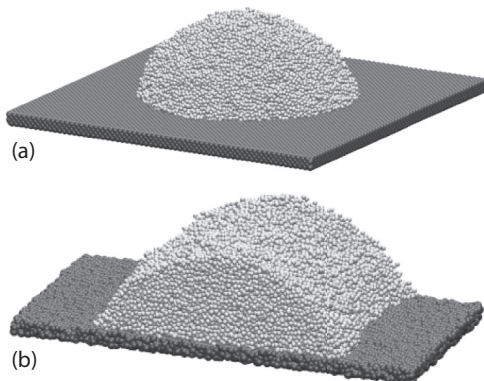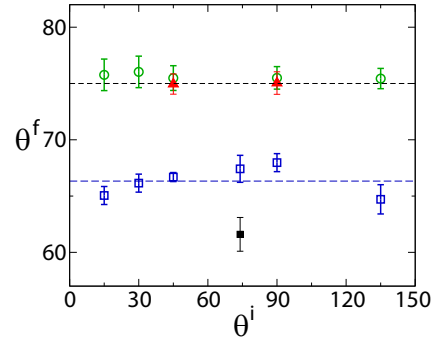

FIG. 2. Geometries used to calculate the contact angle θ. (a) A spherical drop (light) on a rigid crystalline substrate (dark). The height of the drop is $\sim 23\sigma$ and the radius of its base circle is $\sim 31\sigma$. (b) A liquid cylinder (light) on a rigid amorphous substrate (dark). The height of the cylinder is $\sim 21\sigma$, the length 47.6σ, and the width at its base $\sim 60\sigma$.

TABLE II. Contact angles for solid geometries and fluid-solid interaction energies used in simulations.

Solids	ϵ_{fs}/ϵ	Contact angle (deg)
Substrate or commensurate tip	0.8	75
Substrate or commensurate tip	1.08	12
Stepped tip	0.8	75
Amorphous tip	0.8	66.3
Incommensurate tip	0.8	61.6

the commensurate tip. We take the same value for the stepped tip, though the contact angle may be different on terraces and terrace edges. Atoms in the incommensurate tip have the same LJ interaction with fluid beads as those in the commensurate tip, but the incommensurate tip has a slightly higher density, which leads to stronger adhesion and a slightly lower angle $\theta = 61.6°$. The amorphous surface has an intermediate angle of 66.3°.

The zero of tip-substrate separation h is somewhat ambiguous at atomic scales. The separation between the centers of the closest atoms on the tip and substrate will be defined as h_a. The space available to liquid atoms is smaller because of the repulsive excluded volume interactions from each solid wall. We determine the width h_{ex} of the excluded layer near each wall so that the volume available to liquid atoms is consistent with the continuum expression for $h = h_a - 2h_{ex}$. First the liquid density is calculated as a function of distance from the wall. There are strong oscillations near the walls due to the liquid layering described below and in previous work [47–50]. These oscillations decay quickly to a constant density $\rho_0 \sim 0.905m/\sigma^3$. The value of h_{ex} is calculated by requiring that the integral over the oscillatory density from the wall to some central height z is equal to $\rho_0|z - h_{ex}|$. As long as z is in a region with constant density ρ_0, it does not affect the value of h_{ex}. For the substrate and commensurate tip, $h_{ex} = 0.775\sigma$ at zero pressure. Changes with pressure and tip geometry (incommensurate and amorphous) are too small ($<0.1\sigma$) to affect the figures below. Therefore, we take $h_{ex} = 0.775\sigma$ for all the solid walls below.

All simulations were performed using the large-scale atomic-molecular massively parallel simulator (LAMMPS) developed at Sandia National Laboratories [85,86]. Interatomic forces are calculated with the help of neighbor lists. A velocity-Verlet algorithm with a time step $dt = 0.005\tau$ is used to integrate the equations of motion. Constant temperature ($T = 0.7\epsilon/k_B$) is maintained with a Langevin thermostat with damping rate $\Gamma = 0.1\tau^{-1}$.

Since the tip-substrate interaction is truncated at $r_c = 2^{1/6}\sigma$, there is no direct van der Waals attraction between solids. This attraction would be $-AR/6h^2$, where R is the tip radius and A a Hamaker constant [30]. Estimates of this force are smaller than the capillary forces in the examples shown below and decrease much more rapidly as h increases. As discussed by de Gennes [44], van der Waals attractions also produce disjoining pressures that alter the interfacial shape but generally have a small effect unless the contact angle is near zero (perfect wetting). The effect of van der Waals forces on capillary bridging and forces can be taken into account in continuum theories using a mean-field approach or an effective interface potential [46,87].

In our first simulations the capillary force F_{cap} was calculated as a function of h while the tip was brought toward and then away from the substrate at a constant velocity v. As shown in Fig. 4, the resulting force strongly depends on the rate and direction of motion. The hysteresis between approach and retraction increases as h decreases and v increases. For most cases, it is even larger than the equilibrium force that we wish to calculate. Similar results are observed for other tips and liquid bridges.

One source of the hysteresis is the time required for fluid flow to equalize the pressure in the drop. From continuum
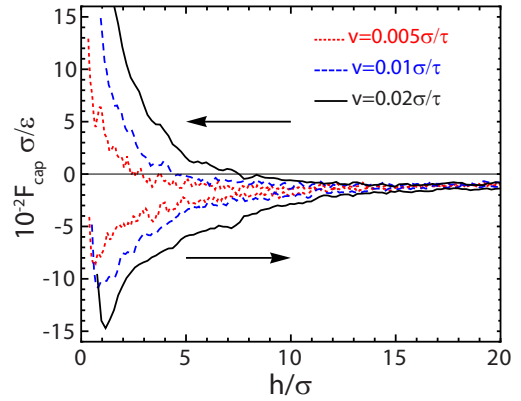

FIG. 4. (Color online) Force-separation curves for the amorphous tip with $R = 100\sigma$ show hysteresis as the tip is displaced at a constant velocity v (legend) toward (h decreases as indicated by the left arrow) and away from (h increases as indicated by the right arrow) the substrate. The volume of the liquid bridge is $V_l = 4.123 \times 10^4\sigma^3$.

lubrication theory, the force required to displace a viscous fluid between a sphere and substrate scales as $F_{visc} \sim 6\pi R^2\eta v/h$, where η is the viscosity [88,89]. Our results are qualitatively consistent with this scaling, although deviations grow at small h where confinement may change the viscosity [69,90,91]. The force is also affected by the finite volume of the drop and the dynamics of the contact line on the two solid surfaces [92].

To resolve forces with the desired accuracy would require decreasing the velocity by two orders of magnitude or more relative to the lowest v in Fig. 4. While such velocities ($v = 5 \times 10^{-5}\sigma/\tau \sim 1$ cm/s) are still orders of magnitude faster than normal velocities in typical AFM experiments, they are very hard to achieve with MD simulations. We find it more efficient to decrease h in small steps and allow the fluid to relax before obtaining statistical averages of local and global forces. The required relaxation time increases as h decreases and/or R increases. We find negligible hysteresis with an equilibration time of 1000τ for $h \gtrsim 1.5\sigma$. At smaller separations the fluid enters a glassy state and the results are not reversible on any accessible time scales. Similar glass transitions have been observed in surface force apparatus (SFA) experiments [90,93,94] and simulations [69,78,95–97].

IV. RESULTS AND DISCUSSION

A. Effects of substrate elasticity

Figure 5 compares force-separation curves for the incommensurate tip with elastic and rigid substrates. In both cases the changes in h reflect the displacement of the rigid tip with respect to the substrate, which is the most accessible quantity in experiments. For elastic substrates the actual change in separation between the closest tip and substrate atoms may be slightly smaller due to compression of the substrate. To remove this effect, h_a is calculated from the closest separation between tip and substrate atoms before the tip contacts the drop. It is then corrected to $h = h_a - 2h_{ex}$ to include the excluded volume effects discussed in the previous section. The value of h is then decreased by the change in tip height as the tip is lowered into contact.
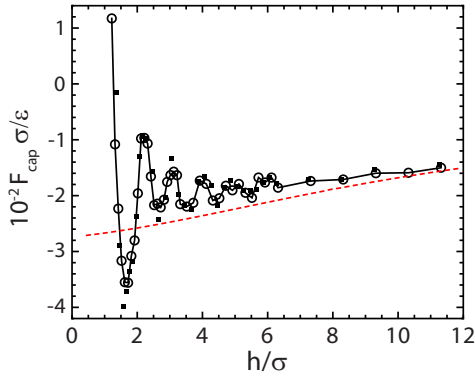
FIG. 5. (Color online) Force-separation curves for the incommensurate tip with $R = 100\sigma$: elastic ($\bigcirc$) vs rigid ($\blacksquare$) substrate. The dashed line is the continuum solution and connecting lines are guides for the eye. The volume of the liquid bridge is $V_l = 4.123 \times 10^4\sigma^3$.

The results for elastic and rigid substrates in Fig. 5 are not evaluated at exactly the same set of h because of the deformability of the elastic substrate, but are consistent within statistical fluctuations for $h > 1\sigma$. At smaller h the dynamics in the liquid bridge become sluggish and large viscous pressures can be generated as the separation is decreased. Substrate elasticity couples to these transients, leading to greater hysteresis between approach and retraction. Since results in this regime are not reproducible, they are excluded from Fig. 5 and subsequent plots, but they may be relevant to experiments.

To understand why substrate elasticity has little effect on capillary adhesion in our simulations we estimate the magnitude of surface deformations using continuum elastic results for a semi-infinite solid. The Laplace pressure will produce a normal displacement of the solid interface. The effective modulus for normal substrate displacements is $E^* \equiv E/(1 - \nu^2)$, where E is the Young's modulus and ν is the Poisson's ratio [98]. The normal strain is thus of order $\Delta p/E^* = \gamma(1/r_1 + 1/r_2)/E^*$. While we have chosen to use a relatively compliant solid, the ratio $\gamma/\sigma E^* \sim 4 \times 10^{-3}$. Since typical radii of curvature in our simulations are larger than 10σ, i.e., $\sigma/r \sim 0.1$, the strains produced at the surface are only of order 10^{-4} [99]. Using results from contact mechanics [98], one finds that the mean displacement of a semi-infinite substrate from the constant pressure $\Delta p = \gamma(1/r_1 + 1/r_2)$ on a circle of radius a is $16(a/r_1 + a/r_2)\gamma/3\pi E^*$. In our simulations a, $|r_1|$, and $|r_2|$ are all of the same order, so the predicted displacement is only of order 0.01σ and relatively constant across the liquid-solid interface. It thus has little effect on force curves. Deformation may be more important for small drops between tips with macroscopic radii, where $a \sim |r_2| \gg |r_1|$.

The meniscus also exerts a force in the region near the contact line. The local pressure is of order γ/ξ, where ξ is the width of the liquid-vapor interface [75]. For our fluids $\xi \sim 4\sigma$. While the corresponding pressure is larger than the Laplace pressure, the resulting strain is still only $\sim 10^{-3}$. Since it enters over a narrow strip around the circumference, its net effect on the substrate displacement is of the same order as the Laplace contribution and negligible in our simulations.

Given the observed equivalence between simulations with rigid and elastic walls, and the estimates of elastic effects from the macroscopic theory, the remainder of the paper will focus on results for rigid walls. We have verified that all the trends and conclusions reached are consistent with additional simulations with elastic walls as long as $\gamma/E^* \ll \sigma$. This condition is typically met for atomistic solids, but the length γ/E^* can be quite long for elastomers. Their modulus is determined by the crosslink density and can be reduced to extremely low values. As shown in recent experiments and simulations, surface tension dominates on lengths less than γ/E^* and can lead to large surface deformations [100–103]. Elastomers only act like elastic solids above the crosslink spacing which is typically several nanometers for systems with large γ/E^*. The deviations from elasticity at smaller scales would affect capillary forces at the small surface separations considered here.

B. Trends with tip radius and liquid bridge volume

Figure 6 shows force-separation curves for tips with different radii and for liquid bridges with two different volumes V_l. Commensurate tips are used in all cases to ensure that the changes are not due to the difference in the tip structure. We have also confirmed that the results represent steady state behavior. In particular, as illustrated in the inset of Fig. 6(a), data taken during the approach and retraction of the tip are consistent within the statistical fluctuations.

There is a strong increase in the magnitude of the capillary force with tip radius that can be understood from macroscopic theory. A larger tip radius means that the separation between solid surfaces changes more slowly with distance from the tip center. For a fixed V_l, the smaller average height means that the drop spreads to larger contact radii a_i and the radius of curvature r_1 decreases (Fig. 1). The Laplace pressure contribution to F_{cap} becomes more strongly attractive because the pressure acts over a larger area and the reduction in r_1 makes the pressure more negative. The increase in a_i also increases the circumference of the circle where the surface tension provides an attractive contribution to F_{cap}.

In general, we find that the macroscopic theory provides an accurate description of F_{cap} for separations bigger than some h_m, where the subscript m indicates *macroscopic*. The length scale at which the percentage error exceeds our statistical errors ($\sim$1%–3%) decreases as the tip radius increases at a fixed V_l. For example, for the larger liquid bridge with $V_l = 4.123 \times 10^4\sigma^3$, h_m drops from about 20σ to less than 10σ as R increases from 100σ [Fig. 6(a)] to 400σ [Fig. 6(b)]. There is also a decrease in h_m for the smaller bridge with $V_l = 2.390 \times 10^3\sigma^3$ as R increases from 25σ [Fig. 6(e)] to 100σ [Fig. 6(f)]. This trend is in part due to the rapid growth in the magnitude of F_{cap} with increasing R, which makes it harder to see deviations from the continuum prediction. However, the absolute error may also decrease as R increases. For example, for the larger liquid bridge the absolute error is $\sim 50\epsilon/\sigma$ at $h = 10\sigma$ for $R = 75\sigma$ [Fig. 6(d)], but is reduced to $\sim 20\epsilon/\sigma$ for $R = 100\sigma$ and $\sim 5\epsilon/\sigma$ for $R = 400\sigma$. Decreasing the volume of the liquid bridge at a fixed R tends to reduce h_m, as well as all other dimensions of the drop.

The deviations from macroscopic theory at $h < h_m$ have two forms. Near h_m there tends to be a systematic upward
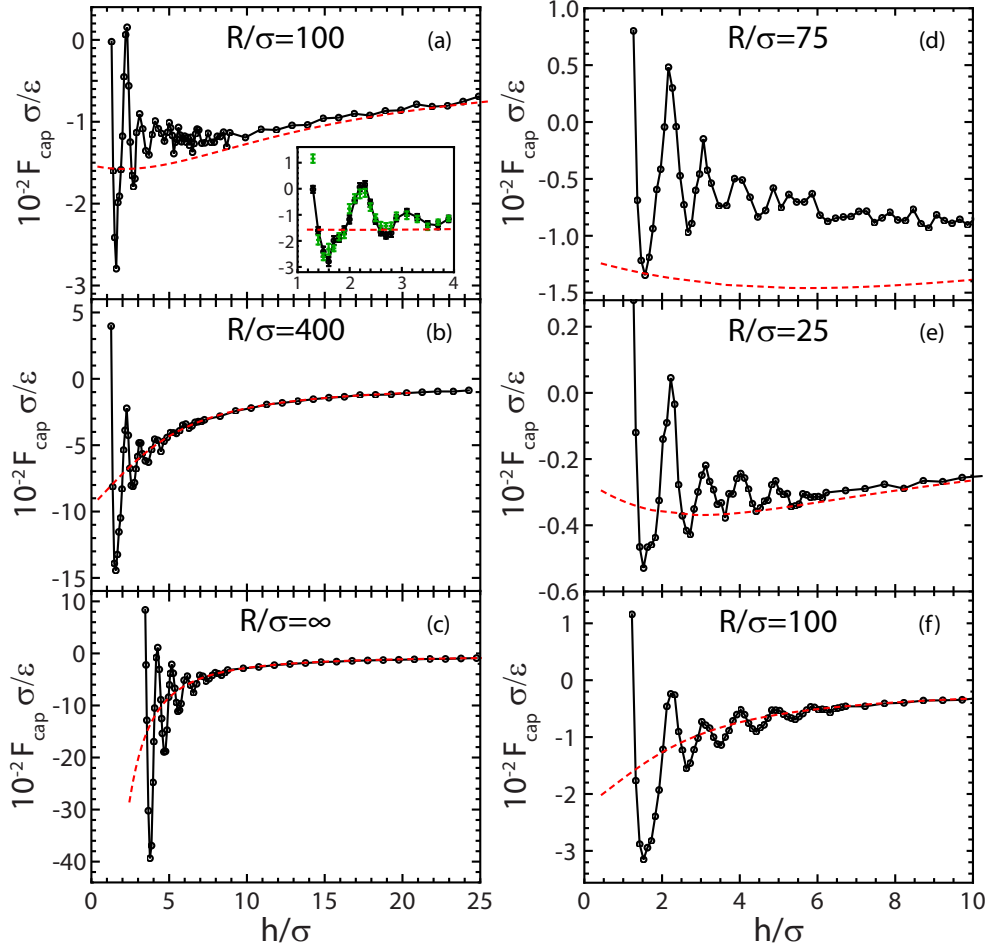
FIG. 6. (Color online) Force-separation curves for commensurate tips with the indicated radii for (a)–(d) a large liquid bridge with $V_l = 4.123 \times 10^4 \sigma^3$ and (e)–(f) a smaller bridge with $V_l = 2.390 \times 10^3 \sigma^3$. The dashed lines are the continuum solutions. The connecting lines are only guides for the eye. Symbols indicate the size of statistical uncertainties. The inset of (a) shows that there is almost no hysteresis in the force between the approach ($\bigcirc$) and retraction (+).

shift in the data that indicates a less adhesive force. At smaller separations there are oscillations in force that grow rapidly in magnitude as h decreases. We denote the length where oscillations become appreciable by h_o where the subscript o indicates *oscillations*. The value of h_o and the magnitude of oscillations tend to be bigger for larger R. The oscillations also become more pronounced and coherent as V_l is reduced.

Force oscillations result from the layering of liquid molecules in the gap between the tip and substrate. This layering was observed in early simulations of flat surfaces [49] and the associated force oscillations were first measured between the nearly parallel plates of an SFA [47]. Recent experiments have found force oscillations for AFM tips with radii of curvature similar to the tips studied here [104]. Layering leads to attractive forces when the separation is slightly larger than an integer multiple of the equilibrium layer spacing, and repulsion when the separation is reduced below this optimal spacing. The alternating of these two regimes produces an oscillatory signature in the force-separation curve.

Figure 7 shows the layered structure of the liquid in the gap between the tip and substrate. The strongest density peaks correspond to layers spaced by $\sim\sigma$ from either the flat wall

or the curved tip. Layering continues into the bulk, but with a decreasing amplitude as the distance from the wall increases. Previous studies of flat surfaces have shown that the range of oscillations is comparable to that of the pair correlation function of the liquid, and that the magnitude of oscillations increases with the magnitude and steepness of the potential from the solid [48–50]. When h is larger than the range of oscillations the central region of the drop behaves like a continuous liquid [Fig. 7(a)]. At smaller h, the layering from opposing surfaces begins to interfere, resulting in the oscillatory forces. A small amount of layering is present throughout the gap at $h = 11.9\sigma$ [Fig. 7(b)] and the layering is pronounced at $h = 1.9\sigma$ [Fig. 7(c)].

The effect of liquid layering on F_{cap} is largest for flat surfaces where the separation is constant across the gap. The curvature of the tip in Fig. 7 leads to variation in the separation between solid surfaces and thus in the number of layers. As a result, the layering force varies in sign and magnitude with ρ, the radial distance from the central axis of the tip, reducing the net contribution to F_{cap}. These observations explain the trends in Fig. 6. The oscillations in F_{cap} decrease with decreasing R because the more rapid changes in separation at small R lead
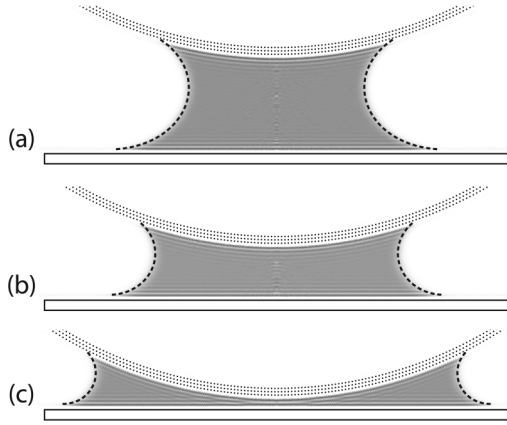
FIG. 7. Layering of the liquid between the tip and substrate for the bent commensurate tip with $R = 100\sigma$ and $\theta = 12°$ at (a) $h = 21.9\sigma$, (b) $h = 11.9\sigma$, and (c) $h = 1.9\sigma$. The gray scale shows the density of liquid as a function of height above the substrate and radial distance from the central axis of the tip. Results are averaged over angles and there is more noise at the tip center because a smaller volume contributes to the average. Dots indicate the positions of tip atoms in a slice through its central axis and dashed lines represent the continuum predictions for the interface profile (Sec. II). The volume of the liquid bridge is $V_l = 4.123 \times 10^4 \sigma^3$.

to cancellation of the layering force from different parts of the tip. Decreasing V_l reduces the range of separations filled by the liquid and thus enhances the force oscillations. The local layering forces are discussed further in Sec. IV D.

C. Effects of atomic structure of tip and contact angle

The atomic structure of the tip affects both the macroscopic contact angle and the degree of liquid layering in the gap. Figures 5 and 6(a) are for the bent incommensurate and commensurate tips with $R = 100\sigma$, respectively. The incommensurate tip has a higher density, producing a more attractive potential and a smaller contact angle. As a result, both the continuum solution and simulation results show a more attractive capillary force for the incommensurate tip. The magnitude of oscillations is similar until $h < 4\sigma$, where it rises more rapidly for the commensurate tip. This difference reflects the stronger in-plane order induced by two commensurate surfaces. Fluid monomers tend to order epitaxially with atoms centered over favorable sites along the substrate. When the epitaxial order induced by both walls adds coherently, as in the gap between two atomic lattices commensurate to each other, the force oscillations become stronger and a crystalline order may even be induced in the fluid [48].

Figure 8 shows results for the stepped and amorphous tips with $R = 100\sigma$ and the large liquid bridge with $V_l = 4.123 \times 10^4 \sigma^3$. Results for the stepped tip lie close to the continuum solution for the same contact angle ($\theta_t = 75°$) as the curved commensurate tip. The smaller contact angle ($\theta_t = 66.3°$) for the amorphous tip leads to larger adhesion, though smaller than for the incommensurate tip ($\theta_t = 61.6°$).

Changes in the atomic structure of the tip lead to more pronounced variations in the oscillatory forces from layering. While the stepped and bent commensurate tips have the same
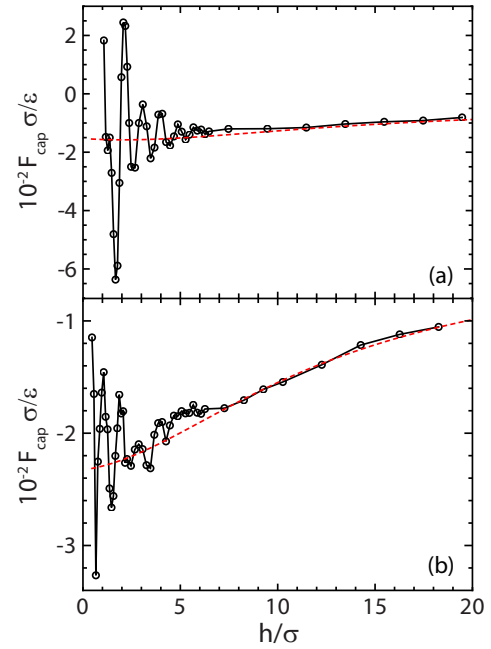

FIG. 8. (Color online) Force-separation curves for (a) the stepped tip and (b) the amorphous tip with $R = 100\sigma$ and the large liquid bridge with $V_l = 4.123 \times 10^4 \sigma^3$. Note that the magnitude of oscillations is about three times smaller for the amorphous tip.

contact angle, the stepped tip gives much stronger oscillatory forces. The reason is evident from Fig. 9. The surface of the stepped tip consists of terraces with fixed separation from the substrate, and the terrace spacing is close to the layer spacing. Thus the layering forces tend to add coherently over the tip surface rather than oscillate as a function of ρ and partially cancel each other. Note that for the stepped tip the size of terraces is not unique for a given tip radius. For the case shown here, the first terrace has radius 8.9σ, but smaller and larger
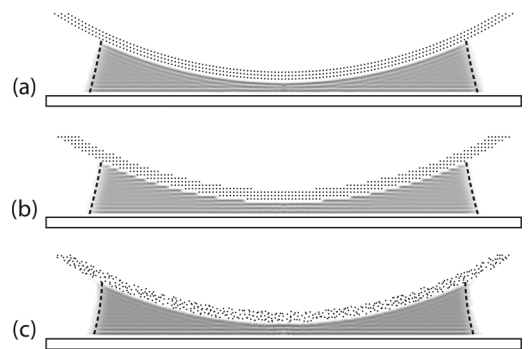

FIG. 9. Layering of liquid molecules in the gap between the substrate and various tips with $R = 100\sigma$ and $V_l = 4.123 \times 10^4 \sigma^3$: (a) the commensurate tip at $h = 2.30\sigma$, (b) the stepped tip at $h = 2.27\sigma$, and (c) the amorphous tip at $h = 2.26\sigma$. The gray scale shows the density of liquid as a function of height above the substrate and radial distance ρ from the central axis of the tip. Results are averaged over angles and there is more noise at the tip center because a smaller volume contributes to the average. Dots indicate the positions of tip atoms in a slice through its central axis and dashed lines represent the continuum predictions for the interface profile (Sec. II).
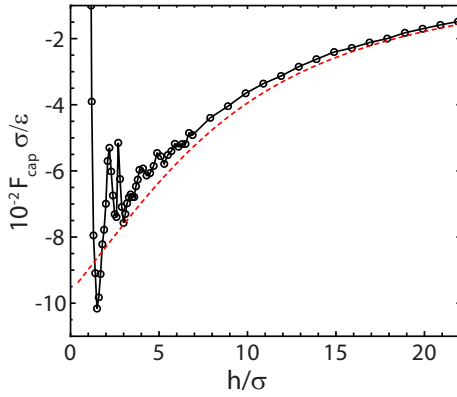
FIG. 10. (Color online) Force-separation curve for the commensurate tip with $R = 100\sigma$, $V_l = 4.123 \times 10^4\sigma^3$, and contact angles $\theta_t = \theta_s = 12°$.

values can be obtained by varying the position of the center of the sphere used to cut the solid into a tip. These variations will change the magnitude of force oscillations and there should be similar variations between crystalline AFM tips with the same nominal radius.

In contrast to the stepped tip, the random roughness on the amorphous surface suppresses force oscillations. Even though height variations are less than one atomic diameter, they are sufficient to change the magnitude and sign of the layering force. The force oscillations nearly cancel except for tip separations that accommodate less than two or three liquid layers (i.e., $h < 3\sigma$).

The changes in contact angle with tip structure in Fig. 8 are relatively small (Table II) because ϵ_{sf} is held fixed. Figure 10 shows F_{cap} vs h for the commensurate tip with $R = 100\sigma$ when θ_s and θ_t are both reduced to 12° by increasing ϵ_{fs} from 0.8ϵ to 1.08ϵ. Both the continuum prediction and the MD results for F_{cap} increase in magnitude by a factor of about 4. This increase can be understood as follows. Comparing Fig. 9 to Fig. 7, it is clear that the radius of curvature r_1 has a much smaller magnitude for $\theta = \theta_t = \theta_s = 12°$. For $\theta < \pi/2$, the radii of curvature r_1 and r_2 have opposite signs with $r_1 < 0$ and $r_2 > 0$. At a large θ in this range (e.g., the case with $\theta = 75°$), $|r_1|$ is large and the magnitude of $\Delta p = \gamma(1/r_1 + 1/r_2)$ is small and may even be positive, giving a repulsive contribution to F_{cap} in Eq. (3) and counteracting the surface tension term. The net result is reduced capillary adhesion. For $\theta = 12°$, $-r_1 \ll r_2$ and the large negative Δp gives a strong attractive contribution to F_{cap} that enhances the attractive meniscus force and leads to large capillary adhesion.

The deviations of the MD results from the macroscopic theory in Fig. 10 for $\theta = 12°$ are comparable to those in other figures shown previously for $\theta = 75°$. Once again the capillary force shows oscillations at $h < h_o \sim 5\sigma$ and is less attractive for $h < h_m \sim 15\sigma$. We now consider the origins of these differences quantitatively.

D. Components of capillary force

As introduced in Sec. II, the macroscopic theory expresses F_{cap} in terms of meniscus and Laplace pressure terms. Both depend on the shape of the interface through the radius of the
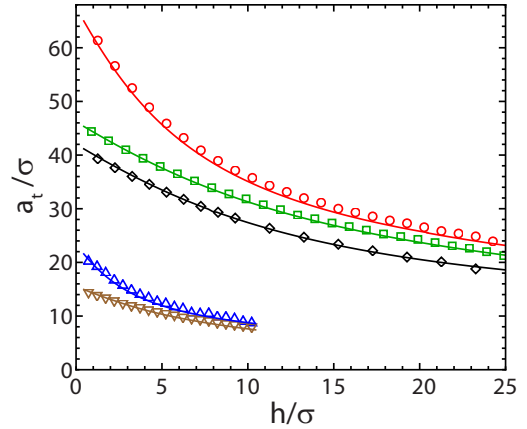

FIG. 11. (Color online) Radius of the contact line on the commensurate tip for some of the cases in Fig. 6. The contact angles are $\theta_t = \theta_s = 75°$. The top three data sets are for the large liquid bridge ($V_l = 4.123 \times 10^4\sigma^3$) and tips with $R = 75\sigma$ (black diamond), $R = 100\sigma$ (green square), and $R = 400\sigma$ (red circle). The bottom two data sets are for the small liquid bridge ($V_l = 2.390 \times 10^3\sigma^3$) and tips with $R = 25\sigma$ (brown downward triangle) and $R = 100\sigma$ (blue upward triangle). Solid lines show the continuum predictions.

contact circle a_i and the interface curvature described by r_i. Figures 7 and 9 include comparisons of the interface shape from simulations with the continuum predictions (dashed lines). Within the intrinsic uncertainty due to the interface halfwidth ($\sim$1–2σ), the macroscopic theory is in excellent agreement with the simulations. Thus the radii of curvature r_i that determine the capillary pressure in the macroscopic theory are consistent with the simulation results.

Figure 11 shows that the simulation results for a_t (the radius of contact circle on the tip surface) also agree with the macroscopic theory. The radius a_t is computed from either the first moment of the probability that a tip atom interacts with the fluid or by the ratio between the first and second moments. It is then corrected for the interaction range. The difference in results from these analysis methods is less than 0.5σ, which is comparable to the largest deviations from the macroscopic theory. The finite width of the interface appears to lead to a very small outward shift in the radius a_t, but this shift is too small to explain the observed deviations from the continuum predictions of the capillary force.

Since the interface shape, including a_t and a_s, is consistent with the macroscopic theory, there must be other factors that lead to the observed shift in the total capillary force from the continuum prediction. These could be deviations in the Laplace pressure Δp or the liquid-vapor interfacial tension γ, or other contributions not captured in macroscopic theory. In Sec. IV B we have discussed force oscillations at small h and related them to layering of the liquid in the gap between the tip and substrate. Here we make this analysis more quantitative. Since the local separation increases continuously with lateral distance ρ from the center of the gap, the layering of liquid also varies with ρ, as does the local force between the liquid bridge and wall. We determine the local force by calculating the total vertical force from liquid atoms on each atom of the flat substrate and use the center of the wall atom as the
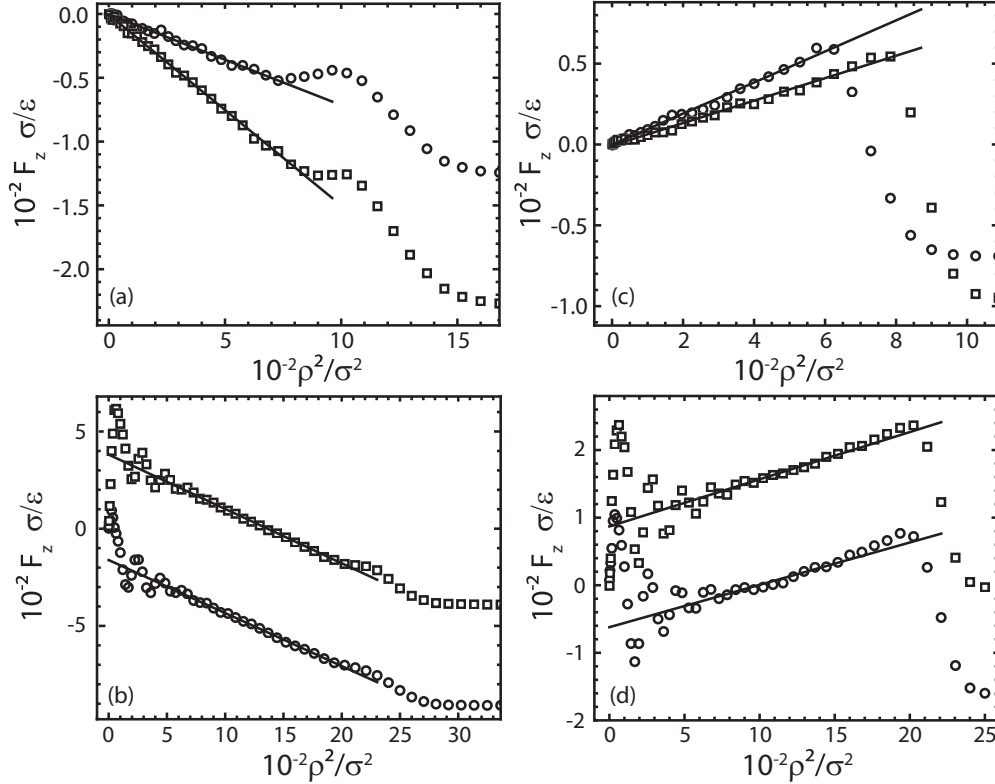
FIG. 12. Integral of the vertical force $F_z(\rho)$ within a circle of radius ρ vs ρ^2 for the commensurate tip with $R = 100\sigma$ and the large liquid bridge with $V_l = 4.123 \times 10^4 \sigma^3$. The left panels are for $\theta_t = \theta_s = 12°$ at various tip-surface separations: (a) $h = 24.9\sigma$ (○) and 15.9σ (□); (b) $h = 1.4\sigma$ (○) and 1.3σ (□). The right panels are for $\theta_t = \theta_s = 75°$ at various tip-surface separations: (c) $h = 24.9\sigma$ (○) and 15.9σ (□); (d) $h = 1.4\sigma$ (○) and 1.2σ (□). The linear fits give a slope πP_n that varies slowly with h and an offset F_{in} that oscillates rapidly with h.

location of the force. Our method for analyzing the net effect of oscillations is illustrated for the commensurate tip with $R = 100\sigma$ in Fig. 12. Results are shown for contact angles $\theta_t = \theta_s = 75°$ and $\theta_t = \theta_s = 12°$, which give different signs for the Laplace pressure.

In Fig. 12, rather than plotting the local force directly, the integral of the vertical force $F_z(\rho)$ from the liquid bridge on substrate atoms within a circle of radius ρ around the central axis of the tip is shown as a function of ρ^2. Using the integrated force reduces noise and separates different contributions to the calculated capillary force. At the outer edge of the contact there is a strong attractive contribution from the liquid-vapor interfacial tension. At smaller ρ, the slope of the curve gives the normal pressure acting on the substrate, $P_n = \frac{1}{\pi} \frac{\partial F}{\partial \rho^2}$. When the tip-substrate separation h is large, $F_z(\rho)$ grows linearly with area $\pi\rho^2$ until the liquid-vapor interface is reached, indicating a constant normal pressure P_n between the liquid bridge and wall. When h gets smaller than h_m, oscillations of $F_z(\rho)$ with ρ^2 are obvious in the central region of the gap where ρ is small. At larger ρ there is a constant normal pressure again and $F_z(\rho)$ grows linearly with area. For the more wetting walls ($\theta_t = \theta_s = 12°$), $F_z(\rho)$ decreases with ρ^2, indicating a negative Laplace pressure and an attractive contribution to F_{cap}. For the same tip and V_l but with $\theta_t = \theta_s = 75°$ the Laplace pressure is positive, i.e., repulsive.

Linear fits in Fig. 12 allow us to extract a slope corresponding to a mean normal (vertical) pressure P_n at intermediate ρ and an offset F_{in} associated with the total contribution of

the layering forces in the central region. As shown in Fig. 12, P_n and its contribution to the capillary force, $F_p = P_n \times \pi a_t^2$, vary slowly with h, as expected from the macroscopic theory. However, F_{in} oscillates rapidly at small h and it is this term that makes up the oscillatory part of F_{cap}.

Using the fits illustrated in Fig. 12 three contributions to the capillary force can be identified,

$$F_{cap} = F_{in} + F_p + F_s, \tag{7}$$

where $F_s = 2\pi a_t \gamma \sin\phi_t$ is the contribution from the interfacial tension around the circumference of the meniscus. Since the macroscopic theory provides an excellent description of the interface shape, it gives accurate values of ϕ_t as well as a_t (Fig. 11). Values of F_s obtained by using either the fit or predicted values of ϕ_t and a_t and from $F_s = F_{cap} - F_{in} - F_p$ are equivalent within statistical errors. The latter is used in plotting the three separate components of F_{cap} in Fig. 13. Consistent values of F_p were also obtained from the fit P_n with either directly measured a_t or the value of a_t calculated with the macroscopic theory.

Figure 13 shows the three components of F_{cap} for two contact angles, $\theta_t = \theta_s = 12°$ and $75°$. The surface contribution F_s is consistent with the continuum prediction for h down to 0.5σ for all cases considered. The underlying reasons are that the interface shape is correctly described by macroscopic theory and the interfacial tension γ of the liquid-vapor interface remains near the bulk value. The latter was confirmed by independent direct calculations of γ as a function of curvature
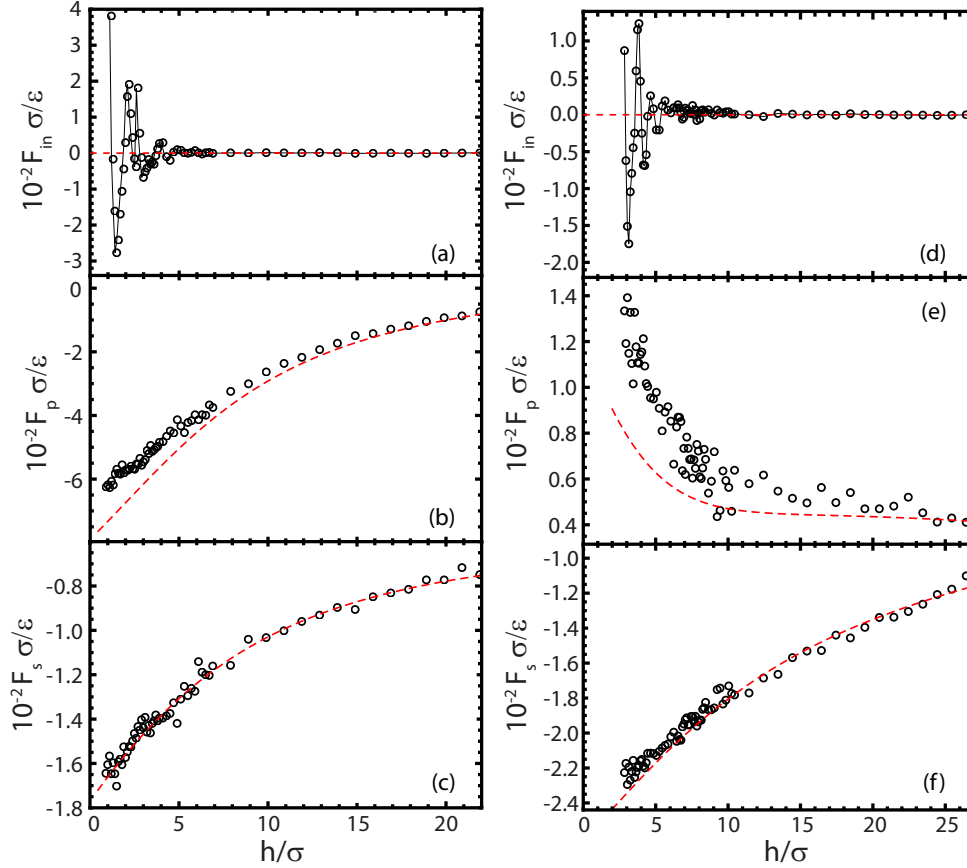
FIG. 13. (Color online) Three components of F_{cap} for the commensurate tip with $R = 100\sigma$, the large liquid bridge with $V_l = 4.123 \times 10^4\sigma^3$, and (a)–(c) contact angles $\theta_t = \theta_s = 12°$ or (d)–(f) contact angles $\theta_t = \theta_s = 75°$. Panels (a), (d) show the oscillatory component F_{in} from the layering force, (b), (e) show the Laplace pressure component F_p, and (c), (f) show the liquid-vapor interfacial tension component F_s.

and distance from a solid wall. It is also clear that the fluid film is thickest at the circumference of the meniscus, which limits atomistic effects at the interface.

The deviations from macroscopic theory are all associated with pressure deviations that contribute to F_{in} and F_p. F_{in} is only significant for the range of $h < h_o \approx 6\sigma$, where the total force shows oscillations. The oscillations have a larger magnitude for the more wetting case that also has stronger wall-fluid interactions. They represent variations in the ease of packing discrete atoms between the confining walls and are not included in the macroscopic theory.

The contribution from the Laplace pressure in outer regions of the drop, F_p, shows a systematic deviation from the macroscopic theory for $h < h_m \approx 18\sigma$. The observed force is always less attractive than the continuum predictions. The magnitude of the shift is consistent with the systematic deviations in the total forces shown in Figs. 6(a) and 10. For the less wetting case and the commensurate tip with $R = 100\sigma$ the average adhesion is reduced by as much as a factor of 2 [Fig. 6(a)]. The reduction is more pronounced for even smaller tips [Fig. 6(d)].

Given that the macroscopic theory gives the correct interface shape and the surface tension retains the bulk value, the deviation of F_p from the continuum prediction implies a failure of the Laplace equation [Eq. (1)] for the pressure in the outer region of the drop. Note that pressure is a tensor and only

the vertical component, P_{zz}, contributes to F_p and $F_z(\rho)$ in Fig. 12. If the interior of the liquid bridge was isotropic, then the pressure tensor would be hydrostatic: $P_{zz} = P_{xx} = P_{yy}$. However, the confining solids can introduce anisotropy. In the case of thin liquid films, there is commonly a disjoining pressure normal to the film that acts to increase or decrease the thickness [44]. As we now show, the in-plane components of the pressure are quite close to the values predicted by the Laplace equation, but the out-of-plane component that determines F_{cap} is consistently more positive.

We computed the pressure tensor in the liquid bridge directly using an algorithm developed by Denniston *et al.* [105], which is based on an expression for the pressure tensor derived by Irving and Kirkwood [106]. The out-of-plane component P_{zz} and the in-plane component $P_{\rho\rho}$ are averaged over values of ρ that are large enough to avoid pressure oscillations and small enough to be inside the meniscus (Fig. 12). Figure 14 compares the variation in these components of the pressure tensor with the prediction for the Laplace pressure Δp from the macroscopic theory (line) and the measured normal pressure on the solid substrate, P_n. For both contact angles, $P_{\rho\rho}$ is close to the predicted Laplace pressure at all separations. As expected from force balance considerations, P_{zz} is also close to the normal force exerted on the substrate P_n. The pressure anisotropy $P_{zz} - P_{\rho\rho}$ increases as h decreases in exactly the same way that the pressure contribution to F_{cap} deviates from the continuum
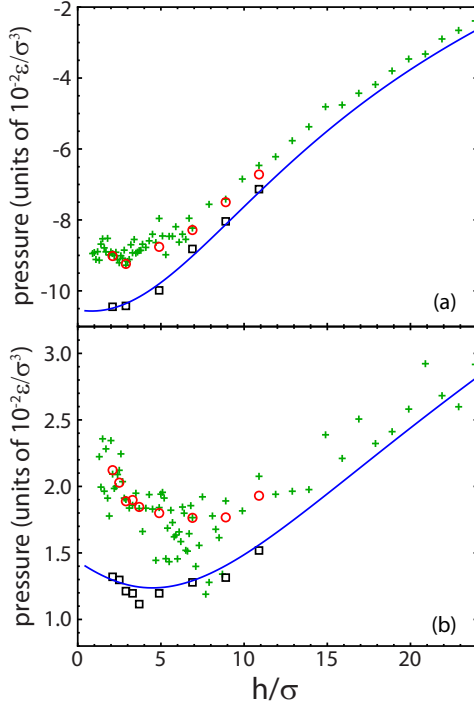
FIG. 14. (Color online) Components of pressure tensor for the commensurate tip with $R = 100\sigma$, $V_l = 4.123 \times 10^4 \sigma^3$, and contact angles (a) $\theta_t = \theta_s = 12°$ and (b) $\theta_t = \theta_s = 75°$. Symbols show the out-of-plane component P_{zz} (red $\bigcirc$) and the in-plane component $P_{\rho\rho}$ (black $\square$) of the pressure tensor in the fluid and the normal pressure on the substrate P_n (green $+$) from the fits shown in Fig. 12. Blue solid lines show the continuum prediction for the Laplace pressure Δp from Eq. (1).

prediction. Similar results were observed with various tips and liquid bridge volumes. As found above, the pressure anisotropy always leads to more repulsive interactions and grows in magnitude as h decreases below about 20σ. For $h < 5\sigma$ it represents a substantial correction to the Laplace pressure contribution to F_{cap}. We conclude that the systematic deviation in F_{cap} from the macroscopic theory results from the pressure anisotropy in the liquid bridge. The physical origin is similar to that giving the disjoining pressure of thin liquid films.

V. SUMMARY AND CONCLUSIONS

In this paper, we used MD simulations to study the capillary forces induced by a liquid meniscus that connects a rigid spherical tip and a flat substrate. We showed that the substrate elasticity has a negligible effect on the total capillary adhesion force, F_{cap}, for most substrates, although new effects may arise for very soft elastomers [100–103]. To reduce computational burden, the substrate is treated as rigid in most simulations reported in this paper.

The value of F_{cap} was calculated as a function of the tip-surface separation h for a range of tip geometries. We showed that if F_{cap} is calculated when the tip is displaced at a constant velocity v, a hysteresis with magnitude depending on v occurs between approach and retraction. To measure equilibrium capillary forces, the separation h is gradually varied and the liquid bridge is allowed to relax to its

equilibrium state at a given h before F_{cap} is computed. As expected, the force-separation curves obtained in this way do not exhibit hysteresis at most separations. However, films that are only one to two layers thick may enter a glassy state that resists equilibration [69,78,90,91]. This immobile layer may affect experimental determinations of the onset of tip-substrate contact.

Our results show that for a typical F_{cap} vs h curve, there exist two critical separations h_m and h_o. The separation h_m is typically about 20σ ($\sim$10 nm) but can vary with the tip radius R and the liquid bridge volume V_l. The separation h_o is roughly 10σ ($\sim$5 nm). When the separation h is larger than h_m, the magnitude of F_{cap} grows as h decreases and agrees with the continuum prediction. This agreement shows that the macroscopic theory of capillaries works down to surprisingly small scales. When h is smaller than h_o, the adhesion force F_{cap} oscillates strongly with h because of molecular layering in the liquid bridge. At an intermediate separation $h_o < h < h_m$, the adhesion F_{cap} is more positive (less attractive) compared with the continuum prediction. The average adhesion can be reduced from the continuum prediction by a factor of 2 or even change sign.

The magnitude of F_{cap} grows as the tip radius R increases because the Laplace pressure term becomes more attractive (or less repulsive when it is positive) and adds to the meniscus contribution [Eq. (3)]. The oscillations in F_{cap} at small h decrease with decreasing R or increasing liquid bridge volume V_l. The reason is that the changes in local separation between the tip and substrate lead to cancellations of the layering force that is responsible for the oscillations. This cancellation is more pronounced for smaller tips or larger liquid bridges.

For tips with the same R, the atomic geometry affects F_{cap} in two ways. One is by changing the contact angle θ_t. The atomic structure also affects the layering of liquid in the gap between the tip and substrate and thus the layering force contribution to F_{cap}. In general, oscillations in F_{cap} at small h for atomically smooth tips (e.g., the commensurate or incommensurate tips) are more coherent and stronger than those for tips with rougher surfaces (e.g., the amorphous tip). However, the stepped tip leads to even stronger oscillations because the changes in local separation are slower (each terrace is actually flat) than for the corresponding commensurate tip. For the commensurate tip with $R = 100\sigma$, F_{cap} becomes much more attractive when the contact angles θ_t and θ_s are reduced from $75°$ to $12°$. The adhesion becomes stronger because the Laplace pressure contribution to F_{cap} changes from repulsion to attraction, which more than compensates for the reduction of the attractive meniscus contribution.

Direct calculations of the density profile of the liquid bridge indicate that the interface shape is consistent with the macroscopic theory. The radii of contact circles (a_t and a_s) on the tip and substrate surfaces agree with the continuum predictions within an intrinsic uncertainty associated with the half-width of the liquid-vapor interface. Such calculations also show clearly the layering of liquid near the solid walls and the interference of the layering from two walls at small h (Figs. 7 and 9).

Our simulations show that generally F_{cap} contains three contributions: an oscillatory part that originates from the molecular layering force in the inner region of the liquid bridge (F_{in}), a contribution from the liquid-vapor interfacial

tension (F_s), and a contribution (F_p) from the average normal pressure P_{zz}. The inner term F_{in} oscillates between positive and negative values as h varies and is only significant when $h < h_o$. This term represents the change in the free energy of the liquid bridge when h is varied. It is not captured in any macroscopic models developed so far but has been observed in SFA and AFM experiments [47,48,104]. The meniscus contribution F_s agrees with the continuum predictions for h down to the order of 2σ ($\sim$1 nm). This is consistent with the facts that the liquid-vapor interface shape is accurately described by the macroscopic theory and the interfacial tension γ does not change appreciably when the interface approaches the solid wall. The mean normal pressure term F_p agrees with the continuum predictions for $h > h_m$, but becomes consistently more positive (less attractive or more repulsive) when h is reduced below h_m. This shift is found to be due to the anisotropy of the pressure tensor in the liquid bridge. The in-plane component $P_{\rho\rho}$ is consistent with the Laplace pressure Δp predicted by the macroscopic theory. However, it is the out-of-plane component P_{zz} that determines the normal forces on the tip and substrate and thus the pressure contribution to F_{cap}. This term is always more positive than the predicted Δp.

In this paper, we focus on F_{cap} as a function of h. As many experiments indicate, capillary forces also contribute significantly to sliding friction and lead to unusual velocity dependence (dynamics) and time dependence (kinetics) [15–19]. It would be interesting to extend the current study to the cases where the tip is displaced laterally so that the liquid bridge is dragged over the substrate surface. The normal force (adhesion) and lateral force (friction) can be calculated simultaneously and their correlations and variations can be studied. This would help us understand the behavior of capillary forces when surfaces are in relative motion. One example is the stability of granular materials when they are sheared or vibrated.

[1] H. M. Jaeger and S. R. Nagel, Science **255**, 1523 (1992).

[2] H. M. Jaeger, S. R. Nagel, and R. P. Behringer, Rev. Mod. Phys. **68**, 1259 (1996).

[3] L. Bocquet, E. Charlaix, S. Ciliberto, and J. Crassous, Nature (London) **396**, 735 (1998).

[4] S. Herminghaus, Adv. Phys. **54**, 221 (2005).

[5] Y. I. Rabinovich, M. S. Esayanur, K. D. Johanson, J. J. Adler, and B. M. Moudgil, J. Adhes. Sci. Technol. **16**, 887 (2002).

[6] D. J. Hornbaker, R. Albert, I. Albert, A. L. Barabási, and P. Schiffer, Nature (London) **387**, 765 (1997).

[7] R. Albert, I. Albert, D. Hornbaker, P. Schiffer, and A. L. Barabási, Phys. Rev. E **56**, R6271 (1997).

[8] T. C. Halsey and A. J. Levine, Phys. Rev. Lett. **80**, 3141 (1998).

[9] S. Nowak, A. Samadani, and A. Kudrolli, Nat. Phys. **1**, 50 (2005).

[10] M. Scheel, R. Seemann, M. Brinkmann, M. D. Michiel, A. Sheppard, B. Breidenbach, and S. Herminghaus, Nat. Mater. **7**, 189 (2008).

[11] C. Yang, U. Tartaglino, and B. N. J. Persson, J. Phys.: Condens. Matter **18**, 11521 (2006).

[12] B. N. J. Persson, J. Phys.: Condens. Matter **20**, 315007 (2008).

[13] P. J. van Zwol, G. Palasantzas, and J. T. M. De Hosson, Phys. Rev. E **78**, 031606 (2008).

[14] E. Charlaix and M. Ciccotti, in *Handbook of Nanophysics Volume 1*, edited by K. Sattler (CRC Press, Boca Raton, 2010).

[15] M. Binggeli and C. M. Mate, Appl. Phys. Lett. **65**, 415 (1994).

[16] S. Ohnishi and A. M. Stewart, Langmuir **18**, 6140 (2002).

[17] E. Riedo, F. Lévy, and H. Brune, Phys. Rev. Lett. **88**, 185505 (2002).

[18] R. Szoszkiewicz and E. Riedo, Phys. Rev. Lett. **95**, 135502 (2005).

[19] O. Noel, P.-E. Mazeran, and H. Nasrallah, Phys. Rev. Lett. **108**, 015503 (2012).

[20] T. Thundat, X.-Y. Zheng, G. Y. Chen, S. L. Sharp, R. J. Warmack, and L. J. Schowalter, Appl. Phys. Lett. **63**, 2150 (1993).

[21] T. Eastman and D. M. Zhu, Langmuir **12**, 2859 (1996).

[22] R. D. Piner and C. A. Mirkin, Langmuir **13**, 6864 (1997).

[23] R. D. Piner, J. Zhu, F. Xu, S. Hong, and C. A. Mirkin, Science **283**, 661 (1999).

[24] X. D. Xiao and L. M. Qian, Langmuir **16**, 8153 (2000).

[25] R. Jones, H. M. Pollock, J. A. S. Cleaver, and C. S. Hodges, Langmuir **18**, 8045 (2002).

[26] L. Sirghi, Appl. Phys. Lett. **82**, 3755 (2003).

[27] A. A. Feiler, J. Stiernstedt, K. Theander, P. Jenkins, and M. W. Rutland, Langmuir **23**, 517 (2007).

[28] S. H. Yang, M. Nosonovsky, H. Zhang, and K. H. Chung, Chem. Phys. Lett. **451**, 88 (2008).

[29] H.-J. Butt, M. Farshchi-Tabrizi, and M. Kappl, J. Appl. Phys. **100**, 024312 (2006).

[30] J. N. Israelachvili, *Intermolecular and Surface Forces*, 2nd ed. (Academic Press, London, 1991).

[31] H.-J. Butt and M. Kappl, Adv. Colloid Interface Sci. **146**, 48 (2009).

[32] F. Dutka and M. Napirkowski, J. Chem. Phys. **124**, 121101 (2006).

[33] A. D. McNaught and A. Wilkinson, *IUPAC Compendium of Chemical Terminology* (Royal Society of Chemistry, Cambridge, UK, 1997).

[34] K. Kocevar, A. Borstnik, I. Musevic, and S. Zumer, Phys. Rev. Lett. **86**, 5914 (2001).

[35] H. Stark, J.-I. Fukuda, and H. Yokoyama, Phys. Rev. Lett. **92**, 205502 (2004).

[36] M. Olsson, P. Linse, and L. Piculell, Langmuir **20**, 1611 (2004).

[37] J. Sprakel, N. A. M. Besseling, F. A. M. Leermakers, and M. A. Cohen Stuart, Phys. Rev. Lett. **99**, 104504 (2007).

[38] K. Bucior, A. Patrykiejew, O. Pizio, and S. Sokolowski, J. Colloid Interface Sci. **259**, 209 (2003).

[39] C. D. Willett, M. J. Adams, S. A. Johnson, and J. P. K. Seville, Langmuir **16**, 9396 (2000).

[40] D. L. Malotky and M. K. Chaudhury, Langmuir **17**, 7823 (2001).

[41] L.-F. Wang, W.-B. Rong, L.-N. Sun, L.-G. Chen, and B. Shao, Chin. Phys. Lett. **26**, 126801 (2009).

[42] Z. Grof, C. J. Lawrence, and F. Štěpánek, J. Colloid Interface Sci. **319**, 182 (2008).

[43] J. S. Rowlinson and B. Widom, *Molecular Theory of Capillarity* (Oxford, London, 1989).

[44] P. G. de Gennes, Rev. Mod. Phys. **57**, 827 (1985).

[45] L. R. White, J. Colloid Interface Sci. **258**, 82 (2003).

[46] F. Dutka and M. Napiórkowski, J. Phys.: Condens. Matter **26**, 035101 (2014).

[47] R. G. Horn and J. N. Israelachvili, J. Chem. Phys. **75**, 1400 (1981).

[48] P. A. Thompson and M. O. Robbins, Phys. Rev. A **41**, 6830 (1990).

[49] S. Toxvaerd, J. Chem. Phys. **74**, 1998 (1981).

[50] J. Magda, M. Tirrell, and H. T. Davis, J. Chem. Phys. **83**, 1888 (1985).

[51] P. A. Thompson, W. B. Brinckerhoff, and M. O. Robbins, J. Adhes. Sci. Technol. **7**, 535 (1993).

[52] F. M. Orr, L. E. Scriven, and A. P. Rivas, J. Fluid Mech. **67**, 723 (1975).

[53] A. Marmur, Langmuir **9**, 1922 (1993).

[54] C. Gao, Appl. Phys. Lett. **71**, 1801 (1997).

[55] A. de Lazzer, M. Dreyer, and H. J. Rath, Langmuir **15**, 4551 (1999).

[56] T. Stifter, O. Marti, and B. Bhushan, Phys. Rev. B **62**, 13667 (2000).

[57] P. Lambert, A. Chau, and A. Delchambre, Langmuir **24**, 3157 (2008).

[58] Any direct interactions between the two solids can be described separately.

[59] L. R. Fisher and J. N. Israelachvili, Nature (London) **277**, 548 (1979).

[60] L. R. Fisher and J. N. Israelachvili, J. Colloid Interface Sci. **80**, 528 (1981).

[61] L. R. Fisher, R. A. Gamble, and J. Middlehurst, Nature (London) **290**, 575 (1981).

[62] M. M. Kohonen and H. K. Christenson, Langmuir **16**, 7285 (2000).

[63] A. C. Mitropoulos, J. Colloid Interface Sci. **317**, 643 (2008).

[64] F. Bresme and N. Quirke, Phys. Rev. Lett. **80**, 3791 (1998).

[65] H. Takahashi and A. Morita, Chem. Phys. Lett. **573**, 35 (2013).

[66] W. J. Stroud, J. E. Curry, and J. H. Cushman, Langmuir **17**, 688 (2001).

[67] J. Jang, G. C. Schatz, and M. A. Ratner, Phys. Rev. Lett. **90**, 156104 (2003).

[68] K. Kremer and G. S. Grest, J. Chem. Phys. **92**, 5057 (1990).

[69] P. A. Thompson, G. S. Grest, and M. O. Robbins, Phys. Rev. Lett. **68**, 3448 (1992).

[70] J. DeConinck, U. D'Ortona, J. Koplik, and J. R. Banavar, Phys. Rev. Lett. **74**, 928 (1995).

[71] J. Rottler and M. O. Robbins, Phys. Rev. E **64**, 051801 (2001).

[72] S. Cheng and G. S. Grest, J. Chem. Phys. **136**, 214702 (2012).

[73] T. Ge, F. Pierce, D. Perahia, G. S. Grest, and M. O. Robbins, Phys. Rev. Lett. **110**, 098301 (2013).

[74] S. Cheng, J. B. Lechman, S. J. Plimpton, and G. S. Grest, J. Chem. Phys. **134**, 224704 (2011).

[75] J. G. Kirkwood and F. P. Buff, J. Chem. Phys. **17**, 338 (1949).

[76] M. P. Allen and D. J. Tildesley, *Computer Simulation of Liquids* (Clarendon Press, Oxford, 1987).

[77] J. Rottler and M. O. Robbins, Phys. Rev. E **68**, 011507 (2003).

[78] S. Cheng, B. Q. Luan, and M. O. Robbins, Phys. Rev. E **81**, 016102 (2010).

[79] B. Q. Luan and M. O. Robbins, Phys. Rev. E **74**, 026111 (2006).

[80] B. Q. Luan and M. O. Robbins, Nature (London) **435**, 929 (2005).

[81] B. Q. Luan, S. Hyun, J. F. Molinari, N. Bernstein, and M. O. Robbins, Phys. Rev. E **74**, 046710 (2006).

[82] N. V. Churaev, V. M. Starov, and B. V. Derjaguin, J. Colloid Interface Sci. **89**, 16 (1982).

[83] J. Gaydos and A. W. Neumann, J. Colloid Interface Sci. **120**, 76 (1987).

[84] F. Dutka and M. Napiórkowski, J. Phys.: Condens. Matter **19**, 466104 (2007).

[85] S. J. Plimpton, J. Comput. Phys. **117**, 1 (1995).

[86] http://lammps.sandia.gov/

[87] D. Andrienko, P. Patrcio, and O. I. Vinogradova, J. Chem. Phys. **121**, 4414 (2004).

[88] G. K. Batchelor, *An Introduction to Fluid Dynamics* (Cambridge University Press, Cambridge, UK, 1967).

[89] S. Cai and B. Bhushan, Nanotechnology **18**, 465704 (2007).

[90] M. L. Gee, P. M. McGuiggan, J. N. Israelachvili, and A. M. Homola, J. Chem. Phys. **93**, 1895 (1990).

[91] S. Granick, Science **253**, 1374 (1991).

[92] A. Borkar and J. Tsamopoulos, Phys. Fluids A **3**, 2866 (1991).

[93] J. Klein and E. Kumacheva, Science **269**, 816 (1995).

[94] A. L. Demirel and S. Granick, Phys. Rev. Lett. **77**, 2261 (1996).

[95] G. He, M. H. Müser, and M. O. Robbins, Science **284**, 1650 (1999).

[96] P. Gallo, M. Rovere, and E. Spohr, J. Chem. Phys. **113**, 11324 (2000).

[97] C. Alba-Simionesco, B. Coasne, G. Dosseh, G. Dudziak, K. E. Gubbins, R. Radhakrishnan, and M. Sliwinska-Bartkowiak, J. Phys.: Condens. Matter **18**, R15 (2006).

[98] K. L. Johnson, *Contact Mechanics* (Cambridge University Press, New York, 1985).

[99] Note that some macroscopic systems can yield through dislocation motion even at such small strains. However, the radii of curvature tend to be larger at these scales and the threshold for plastic flow is higher at submicron scales.

[100] E. R. Jerison, Y. Xu, L. A. Wilen, and E. R. Dufresne, Phys. Rev. Lett. **106**, 186103 (2011).

[101] R. W. Style and E. R. Dufresne, Soft Matter **8**, 7177 (2012).

[102] R. W. Style, R. Boltyanskiy, Y. Che, J. S. Wettlaufer, L. A. Wilen, and E. R. Dufresne, Phys. Rev. Lett. **110**, 066103 (2013).

[103] J.-M. Y. Carrillo and A. V. Dobrynin, Langmuir **28**, 10881 (2012).

[104] S. P. Jarvis, T. Uchihashi, T. Ishida, H. Tokumoto, and Y. Nakayama, J. Phys. Chem. B **104**, 6091 (2000).

[105] C. Denniston and M. O. Robbins, Phys. Rev. E **69**, 021505 (2004).

[106] J. H. Irving and J. G. Kirkwood, J. Chem. Phys. **18**, 817 (1950).